Journal of Materials Chemistry A

ROYAL SOCIETY OF CHEMISTRY

PAPER

View Article Online
View Journal

Cite this: DOI: 10.1039/d4ta01936a

A flexible asymmetric supercapacitor assembled by dahlia-like core–shell cobalt/tin-based chalcogenide@nickel hydroxide grown on reduced graphene oxide†

Huiru Sun,‡[a] Hanwen Zong,‡[a] Wenjun Huang,[a] Lejiao Duan,[a] Jingjing Dong,[b] Yuesheng Sun,[a] Zhongqi Lu,[a] Zhihan Yang,[a] Yawen Liu[a] and Jingquan Liu *[a]

Tin-based chalcogenides are generally supposed to be some of the most promising electrode materials with their unique characteristics like facile synthesis, low cost, and eco-friendliness. Nevertheless, the tin-based chalcogenides have low intrinsic conductivity, severe volume effect and electrochemical driven hysteresis, as applied directly to the materials used as supercapacitor electrodes, impeding additional advancements in their electrochemical properties. Therefore, tin-based chalcogenides, especially stannous sulfide, are less reported in the field of supercapacitors. To alleviate these problems, a dahlia-like stannous sulfide-based composite (rCSCTN) has been achieved by *in situ* growth of dahlia-like core–shell cobalt/tin-based chalcogenide@nickel hydroxide on graphene layers. The synthesis strategy can effectively enhance the electrochemical reaction kinetics of the material for electrodes while also improving the supercapacitor properties of the electrode materials by means of the mechanisms of energy storage active site intervention and multi-component synergistic effect. Furthermore, a PVA/KOH gel-electrolyte can be used to create a malleable and highly tensile rCSCTN/PVA/KOH film electrode that can curve at a variety of angles. The constructed supercapacitor apparatus can operate a multipurpose display for more than 12 min in real-world applications. As a result, this innovative study provides fresh motivation for creating composite electrodes for flexible asymmetric supercapacitors that are based on tin-based chalcogenides.

Received 22nd March 2024
Accepted 2nd September 2024

DOI: 10.1039/d4ta01936a

rsc.li/materials-a

1. Introduction

The progress of human civilization cannot be separated from the development of energy technology from beginning to end, and energy is an important source to promote scientific and technological innovation, social progress and exploration of the unknown by humans.[1–4] As the power basis of daily life and production, fossil energy has been exploited for thousands of years, not only accelerating the development of human society but also paying the price of environmental pollution.[5,6] Behind the bright lights and convenient transportation is the sacrifice of the natural environment, such as air and rivers. Accordingly, because of its clean and sustainable use, green energy has become the only way to develop future energy systems. However, green energy such as wind and photovoltaic energy is derived from nature, but also subject to nature. At the same time, the anticipated nuclear energy industry has not been used on a large scale worldwide at this stage because of its high cost and greater potential risks. Therefore, energy storage has become a key factor in the current development of green energy.[7–9]

Batteries, supercapacitors (SCs) and dielectric capacitors, as a category of electrical energy storage devices, have been widely researched to make efficient utilization of green energy. By contrast, aqueous SCs, as emerging energy storage devices, have attracted strong interest and bridged the power/energy distinction between conventional capacitors with dielectric properties (with large power output) and batteries/fuel cells (with significant energy storage) owing to their distinctive electrochemical characteristics, especially the outstanding safety, low cost and highly conductive electrolytes, substantial power density, outstanding specific capacitance, superb charge–discharge velocity and long-term cycling stability along with favorable electrochemical reversibility.[10–14] Typically, SCs fall into two categories based on the charge storage method.

[a]College of Materials Science and Engineering, Institute for Graphene Applied Technology Innovation, Collaborative Innovation Centre for Marine Biomass Fibers, Materials and Textiles of Shandong Province, Qingdao University, Qingdao 266071, P. R. China

[b]Key Laboratory of Colloid and Interface Chemistry, Ministry of Education, School of Chemistry and Chemical Engineering, Shandong University, Jinan 250100, P. R. China

† Electronic supplementary information (ESI) available. See DOI: https://doi.org/10.1039/d4ta01936a

‡ These authors contributed equally to this work.

Activated carbons (ACs), carbon nanotubes (CNTs) and graphene are instances of electrical double layer capacitors (EDLCs). Pure electrostatic charge deposited on the electrode/electrolyte boundary surface is the primary source of EDLCs.[15–19] Consequently, they heavily depend on the surface area of the material for the electrode that the electrolyte ions may access. The other type consists of pseudo-capacitors (PCs), where electro-active substances such as RuO_2 and MnO_2 induce quick and reversible faradaic reactions. Therefore, compared to EDLCs, where electrostatic adsorption solely takes place at the electrode/electrolyte interface, they have a higher theoretical specific capacity. Depending upon the composition of the electrode materials, these two mechanisms may operate concurrently. Nevertheless, materials made from carbon frequently come with an array of drawbacks, including long ion-diffusion distances (>5 μm) and unpredictable pore size and shape, resulting in unsatisfactory specific capacitance. Given their rapid and reversible redox processes and electrode materials, which are often transition metal oxides/hydroxides and conducting polymers, PCs exhibit higher specific capacitance than EDLCs.[20,21] However, long-term stability remains a weakness for PCs. The inherent instability of some pseudocapacitive materials is caused by the charge-storage mechanisms of PCs, hence compromising the long-term stability of SCs. The inherently very high capacitance of PCs is sometimes overshadowed by their lower cyclical stability.[22] These drawbacks are caused by a variety of intricate factors related to PCs' electronic characteristics, electrochemical behaviors, and structural integrity.[23,24] In order to address the needs of emerging applications like storage on the grid and electric hybrid vehicles, there is currently an increasing requirement for SCs with larger energy densities, greater rate capabilities, and longer cycling lives due to the rapid advancement of technology and science.[25–27] Usually, the performance of a single material cannot meet the requirements of high performance, so development of multi-element composites is a promising alternative.[28,29] Therefore, new SC electrode composites with high performances have been explored extensively.[25]

Among many electrode materials, stannous sulfide (SnS) has become one of the electrode materials with broad application prospects due to its considerable energy storage capacity, low price, rich raw material reserves, low toxicity and low pollution.[30–32] However, it is limited by its poor electrical conductivity and bulk expansion.[33] SnS also shows problems such as sudden drop in circulation capacity, low rate performance and low reaction power, thus not being able to fully play a role in high energy storage.[25] In order to solve these shortcomings, SnS composite materials were created to fully use the benefits of SnS energy storage through the strengthening effect between composite materials.[34–36] Zou *et al.* have reported the synthesis of Co–SnS@CNF composites using electrospinning, hydrothermal technique and annealing treatment, which resulted in a specific capacitance of 750 F g^{-1}.[37] John *et al.* synthesized NiS@SnS@$Ni_3Sn_2S_2$/MWCNT through a facile microwave approach, which delivered a peak capacitance of 766 F g^{-1}.[38] However, the low electrochemical properties of the electrode are caused by the poor ion and electron transport rate of SnS. In order to counteract this drawback, the employment of carbon-based materials as conductors to attain the desirable structural stability and conductivity has ignited an important expectation. Furthermore, as a single material's efficacy is no longer sufficient for manufacturing outstanding-performance SCs, the development of multi-element composite materials with excellent properties for SC electrodes is essential.

Herein, we successfully synthesized a dahlia-like stannous sulfide-based composite by *in situ* growth of dahlia-like core–shell cobalt/tin-based chalcogenide@nickel hydroxide on graphene layers, abbreviated as rCSCTN. Using rCSCTN as an electrode that works in a 6 M KOH electrolyte, a three-electrode system apparatus is used to test the electrochemical characteristics of the produced nanomaterials. At a current density of 1 A g^{-1}, the constructed rCSCTN electrode is found to display a superior capacitance of 1066 F g^{-1} (533 C g^{-1}). In addition, at a high current density of 10 A g^{-1}, the capacitance retention is up to 88.5% after 10 000 cycles. Additionally, a solid-state asymmetric supercapacitor (ASC) apparatus of rCSCTN//AC is developed with exceptional cycling performance of 90.5% after 10 000 cycles at a current density of 10 A g^{-1} and remarkable capacitive performance of 81.1 F g^{-1} (40.55 C g^{-1}) at a current density of 1 A g^{-1}. In the meantime, the constructed ASC device demonstrates potential usefulness for energy storage with an energy density of 26.2 W h kg^{-1} and an associated power density of 748.9 W kg^{-1}, which is capable of lighting up a multi-function monitor for 12 minutes. Moreover, high-strength and pliable rCSCTN/PVA/KOH film electrodes that can be folded at multiple angles were created using a PVA/KOH gel-electrolyte. The rCSCTN/PVA/KOH film is noteworthy for its ability to lift plastic bottles with 500 mL of water, suggesting that it has exceptional potential for usage in wearable and compact electronic gadgets. All things considered, this work offers a crucial method for creating tin-based chalcogenide composites with excellent electrochemical performance for flexible energy storage uses.

2. Results and discussion

As shown in Scheme 1, rCSCTN with a dahlia-like core–shell architecture was successfully prepared by two solvothermal strategies. To take advantage of the robust interplay between graphene nanosheets and core–shell cobalt/tin-based chalcogenide@nickel hydroxide, graphene nanosheets were fabricated by a modified Hummers' method first. Subsequently, cobalt/tin-based chalcogenide@nickel hydroxide was grown on the graphene nanosheets by two facile solvothermal strategies. Finally, by centrifugation and freeze-drying, water is removed, leading to the formation of flexible and conductive dahlia-like architecture of rCSCTN.[39] In order to achieve the dahlia-like core–shell architecture, core–shell cobalt/tin-based chalcogenide@nickel hydroxide is inserted between graphene layers. This not only significantly increases the final product's specific surface area and active sites, but it also skillfully avoids the problem of inadequate ionic and electronic transport in electrode materials, which allows them to fully exhibit their electrochemical performance. On the other hand, the joining of

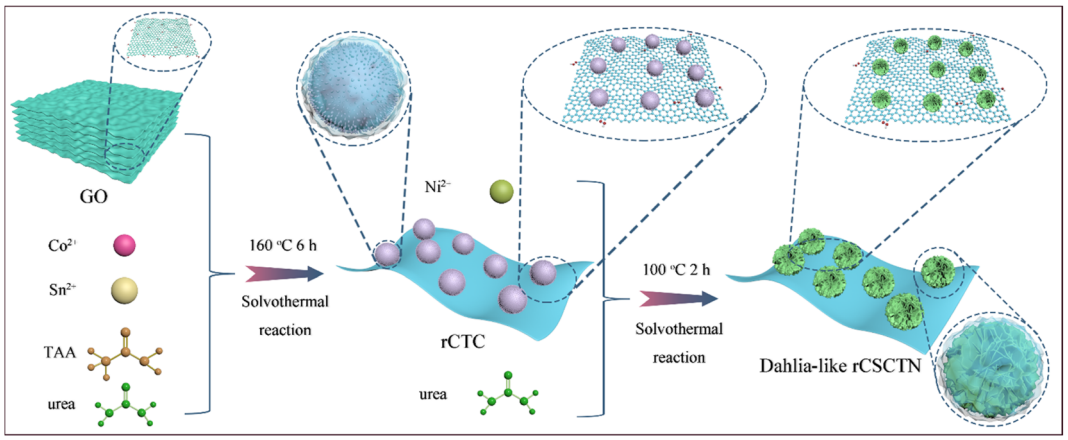

Scheme 1 Diagrammatic representation for stepwise synthesis of rCSCTN.

graphene layers to core–shell cobalt/tin-based chalcogenide@-nickel hydroxide not only greatly increases the electrical conductivity to facilitate redox reaction and charge transfer rates of rCSCTN in the electrochemical process but also stabilizes its structure during charge–discharge cycling processes. The promoting effect of graphene on structural stability can be reflected in the subsequent electrochemical cyclic performance and rate performance. Furthermore, a sizable specific surface area and multiple accessible active sites are offered by the dahlia-like core–shell design, which can greatly enhance electrochemical performances. In conclusion, the resulting dahlia-like, conductive, and flexible composite with a core–shell design is anticipated to be a good fit for a high-performance electrode in energy storage devices.

Utilizing a scanning electron microscope, the morphological and structural properties of rCTC-4 and rCSCTN-1, -2, -3, and -4 were first investigated. As displayed clearly in Fig. 1a–c, rCTC-4 synthesized by the first-step hydrothermal method has a large number of nanospheres uniformly grown on the graphene surface. As seen in Fig. 1d–f, after the second hydrothermal treatment, the obtained rCSCTN-4 with numerous nanosheets stacked on the basis of the original nanospheres presents a typical three-dimensional flower cluster morphology while the other three samples all present poor morphology without lots of active sites as depicted in Fig. S2.† Furthermore, the EDS elemental mapping images of rCSCTN-4 displayed in Fig. 1g show the coexistence of C, Co, Ni, O, S and Sn. Additionally, from Fig. S3† and its inset, the existence, mass and atomic

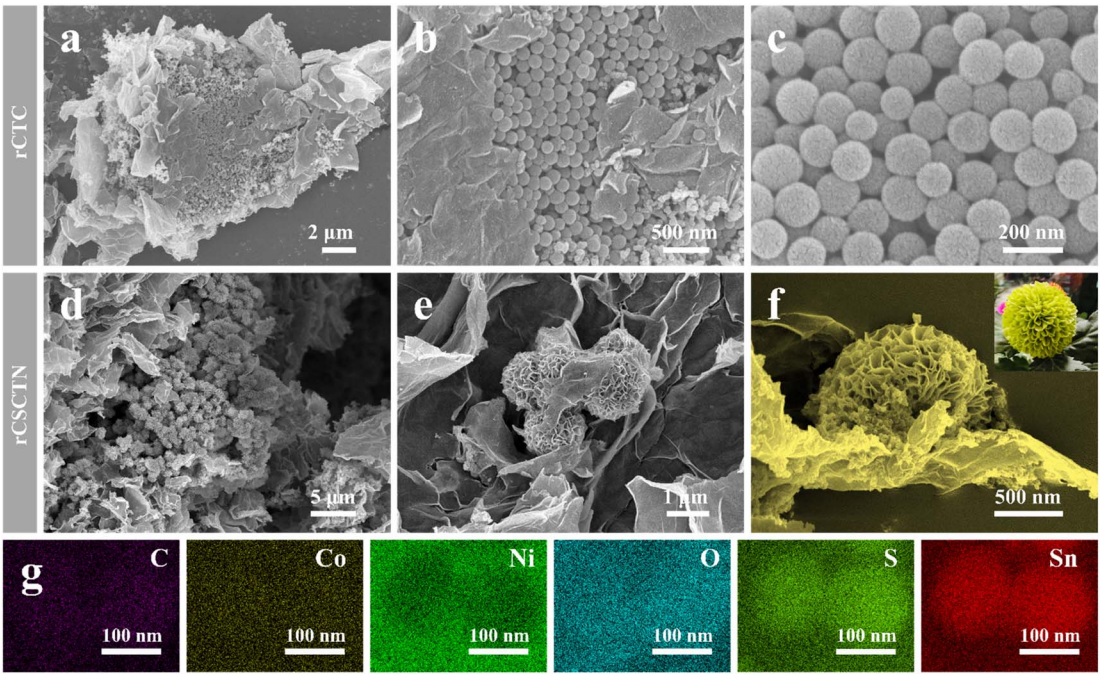

Fig. 1 SEM images of rCTC (a–c) at various magnifications, and (d–f) rCSCTN. (g) EDS elemental mapping images of rCSCTN.

ratios of these elements can also be proved through the EDS spectrum. To sum up, homogeneous nanospheres generated by the first hydrothermal step provide abundant attachment sites for the growth of nanosheets. The specific surface area of the rCSCTN-4 composite is greatly increased by the quantities of nanosheets formed on the surface of nanospheres. This results in abundant active sites for electrochemical reaction and improved capacitance.

TEM, HRTEM, X-ray diffraction (XRD), and element mapping were used to further investigate the internal structure morphologies and chemical composition of rCSCTN. Fig. 2a and b presents TEM images of rCTC, which demonstrate Co/SnS nanoparticles are homogeneously dispersed on graphene sheets. This also lays the foundation for the successful attachment of CSCTN to the graphene. Fig. 2d, e and S4a† clearly show that CSCTN nanoflowers were attached to the graphene surface. The significant increase in particle size proves the successful synthesis of rCSCTN, indicating that the nanosheets have been successfully attached onto the Co/SnS nanospheres. The TEM results illustrated in Fig. 2c and f match those from the SEM images in Fig. 1a–f, respectively. This well-designed core–shell heterostructure endows rCSCTN with abundant accessible active sites, ensuring excellent electrochemical performance. Additionally, the SAED images depicted in the insets of Fig. 2c and f show diffraction rings. Furthermore, the HRTEM images (Fig. 2c and f) of rCSCTN display extremely ordered fringes of the lattice. Its average spacings are 0.283 nm and 0.23 nm, which correspond to the (111), (002), (006), (012), (101), (015), (110), (012), (013) and (102) lattice spacings of rCSCTN. Additionally, the HRTEM image further confirms that both crystalline and amorphous structures coexist in the rCSCTN composite. Among them, rGO is in the amorphous region, and CSCTN is in the crystalline region. As depicted in Fig. 2g, energy dispersive X-ray spectrometry (EDS) reveals the sample contains six elements, namely C, Co, Ni, O, S and Sn, and these elements are evenly distributed throughout the rCSCTN dahlia-like structures. Moreover, Fig. S4b† presents the EDS spectrum, with corresponding proportions and mass of all elements in rCSCTN.

Meanwhile, XRD was used to determine the crystal forms of rCSCTN and rCTC. Six strong diffractions of rCTC at 2θ values of 26.033°, 27.506°, 30.484°, 31.589°, 39.133° and 51.283° were observed in the patterns of SnS (JCPDS no. 01-0984). As shown by the XRD pattern of rCSCTN, distinct peaks were observed at 26.033°, 27.506°, 30.484° and 31.589°, which are well indexed to the (012), (102), (110) and (013) crystal faces of SnS (JCPDS no. 01-0984) respectively, consistent with the HRTEM results. In addition to the diffraction peaks of SnS, typical sharp peaks at 22.735°, 33.458°, 34.412° and 38.765° corresponding to (006), (101), (012) and (015) derived from $Ni(OH)_2$ (JCPDS no. 38-0715) are observed simultaneously with low intensities which may be attributed to the poor crystallinity of $Ni(OH)_2$. Similar results have been reported previously.[40–42] All of the above results indicate the successful synthesis of the core–shell structure, which also correspond to the HRTEM results. Additionally, the interaction impact between $Ni(OH)_2$ and SnS caused the peaks of rCSCTN to dramatically drop, further demonstrating the effective synthesis of the rCSCTN composite.[43]

The chemical bonding states and surface elemental configuration of rCSCTN were characterized *via* XPS. The wide-scan survey XPS spectrum of rCSCTN is displayed in Fig. 3a, which confirms the presence of the elements C, Co, Ni, O, S and Sn. The C 1s spectrum in Fig. S5b† may be deconvoluted into three peaks indexed to C–O/C=O, C–O, and C=O, respectively, at

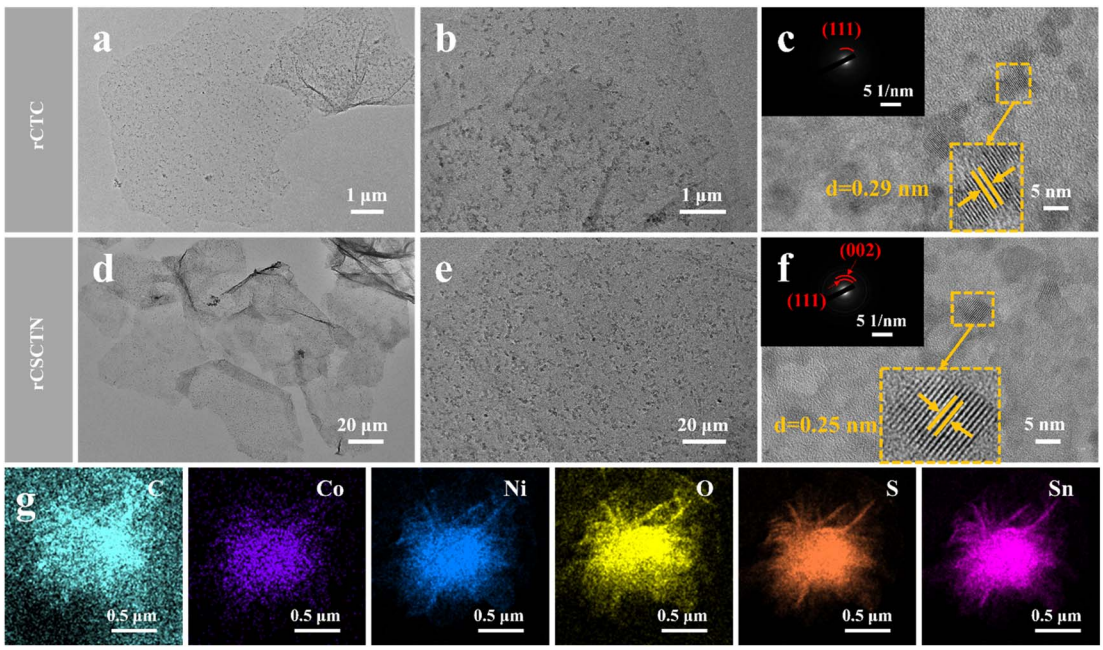

Fig. 2 Images of rCTC: TEM (a and b) and HRTEM (c). Images of rCSCTN: (d and e) TEM and (f) HRTEM. Images of the elements C, Co, Ni, O, S, and Sn from EDS elemental mapping (g).

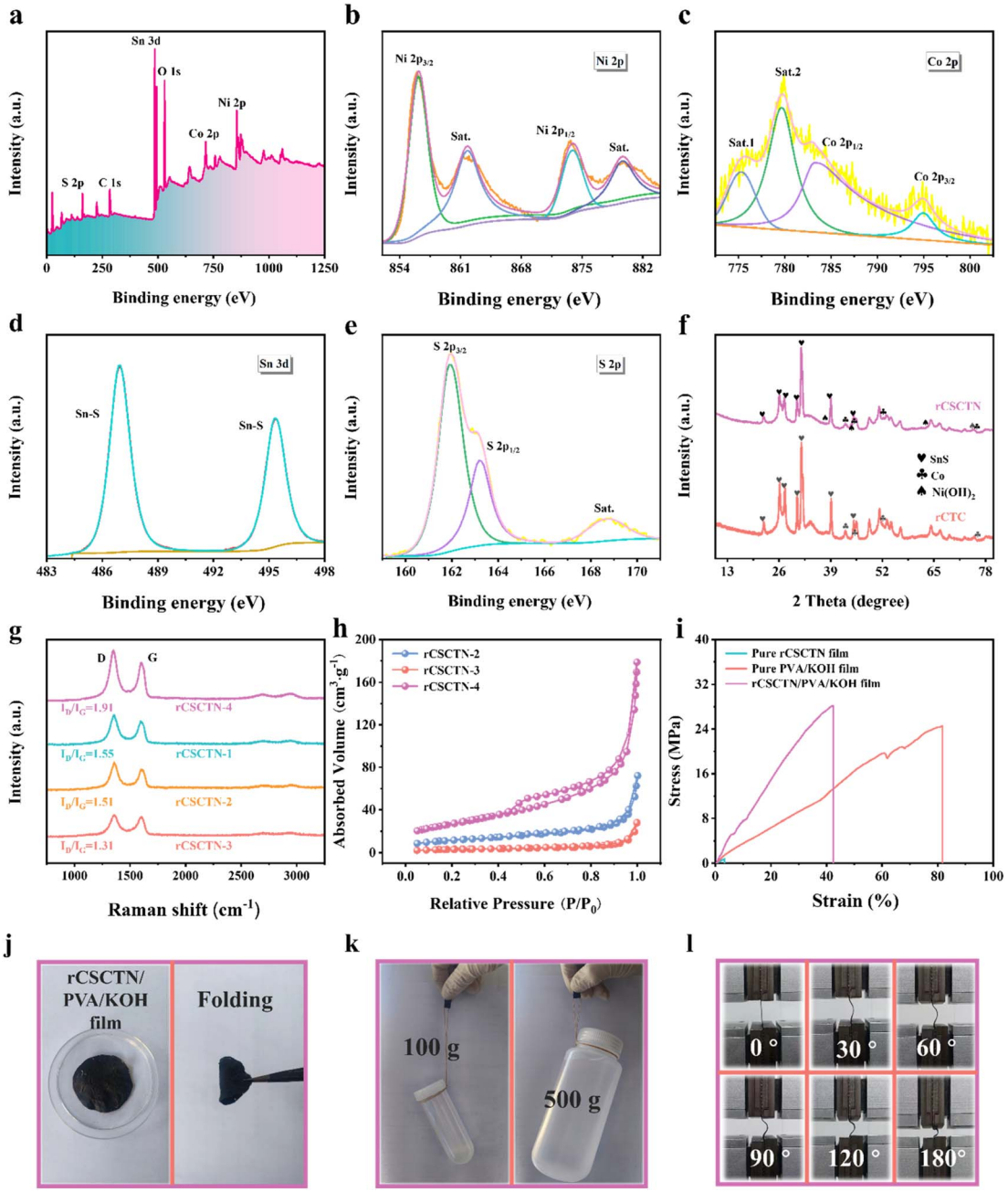

Fig. 3 (a) Survey XPS spectrum and high-resolution spectra for Ni 2p (b), Co 2p (c), Sn 3d (d) and S 2p (e) of rCSCTN. (f) XRD patterns of rCTC and rCSCTN. (g) The Raman spectra of rCSCTN-1, -2, -3 and -4. (h) The nitrogen adsorption–desorption isotherms of rCSCTN-2, rCSCTN-3 and rCSCTN-4. (i) The stress–strain curves of rCSCTN/PVA/KOH composite film, pure PVA/KOH film, and pure rCSCTN film. (j) Images of the rCSCTN/PVA/KOH film and (k) the composite film's tensile strength measurement for a range of weights. Photographs showing the rCSCTN/PVA/KOH film bent at numerous angles (l).

284.88 eV, 286.78 eV, and 289.38 eV. Fig. 3c shows the spectrum of Co 2p.[44] The two peaks at 783.38 eV and 795.08 eV, accompanied by two satellite peaks of Co 2p at 779.68 eV and 775.28 eV, should belong to Co $2p_{3/2}$ and Co $2p_{1/2}$, indicating the presence of Co^{2+} ions.[45,46] A similar phenomenon is noticed in the spectrum of Ni 2p in Fig. 3b. The four peaks that make up Ni 2p include Ni $2p_{3/2}$ and Ni $2p_{1/2}$, which are situated at 856.08 eV and 873.78 eV, respectively, and two satellite peaks, which are placed at 879.5 eV and 862.1 eV, respectively. The binding energy difference between Ni $2p_{3/2}$ and Ni $2p_{1/2}$ is 17.6 eV, in line with α-$Ni(OH)_2$. The O 1s spectrum shown in Fig. S5c† can be well fitted into two primary peaks, corresponding to the O–H and O–Ni functions, at 532.28 eV and 531.28 eV, respectively.[47] As depicted in Fig. 3e, the S 2p spectrum has two peaks, which are situated at 161.98 eV and 163.28 eV for S $2p_{3/2}$ and S $2p_{1/2}$, respectively, along with a satellite peak at 168.78 eV. In Fig. 3d, the binding energies of Sn $3d_{3/2}$ and Sn $3d_{5/2}$ are 495.28 eV and 486.98 eV, respectively.[48]

A Raman spectral analysis was done on rCSCTN-1, -2, -3 and -4 and the profiles are depicted in Fig. 3g to assess the rCSCTN composite's development in more detail. Each sample has a D band (about 1350 cm^{-1}) and a G band (about 1580 cm^{-1}). The D peak is associated with lattice defects in the graphene plane, whereas the G peak is caused by crystalline graphite that forms when graphene is annealed.[49,50] Additionally, the samples exhibit the presence of graphitized π electron state. This explains the appearance of the 2D band for all rCSCTN composites at 2500–3000 cm^{-1}. As can be seen from Fig. 3g, among all the samples, the I_D/I_G value of rCSCTN-4 is the highest, indicating it has the highest degree of defects.[51–53] Moreover, the results of the BET test indicated that a greater porous structure of the rCSCTN composite was also formed. Hence, the high degree of graphitization of rCSCTN-4 facilitates fast electron transfer and greatly enhances electrochemical performance.

Furthermore, Fig. 3h and S6† illustrate the N_2 adsorption–desorption isotherm and the pore size distribution of rCSCTN-2, -3 and -4, correspondingly. The distribution of pore sizes and the specific surface area of the as-prepared rCSCTN-4 composite were quantitatively analyzed by the BET method with rCSCTN-2 and -3 as the reference samples. The specific surface area of rCSCTN-4 was found to be 40.785 $m^2\ g^{-1}$. Moreover, the total volume of pores was 0.096643 $cm^3\ g^{-1}$ and the average pore diameter was 11.263 nm. Significantly, rCSCTN-4's pore volume and specific surface area were greater than those of the other two samples according to Fig. S6.† As a result, the larger specific surface area of rCSCTN-4 facilitates exposure of more active sites and accelerates ion transfer between the electrolyte and electrode materials, promoting electrochemical performance.

In addition to the above examinations, the mechanical characteristics of the rCSCTN/PVA/KOH film, as depicted in Fig. 3i, were studied through tensile testing. As can be obviously seen, the rCSCTN/PVA/KOH film's mechanical property is better in comparison to pure rCSCTN film. This result demonstrated that the addition of PVA (polyvinyl alcohol) significantly improved the tensile strength of the film. Fig. 3j displays an image of the rCSCTN/PVA/KOH film. The method of preparing the film is as follows. To begin with, the as-prepared PVA/KOH hydrogel was evenly applied to the rCSCTN film to allow it to completely infiltrate into the rCSCTN film. In the second place, the film was left at room temperature lasting for 24 hours before being pressed under an intense pressure of 20 MPa for 35 minutes. In addition to the stress–strain test, through lifting real objects, the strength under tension of the rCSCTN/PVA/KOH film was then evaluated. As is demonstrated in Fig. 3k, this composite film demonstrated the ability to support plastic bottles containing 500 mL (500 g) and 100 mL (100 g) of water. Additionally, the rCSCTN/PVA/KOH film can be bent at different angles (Fig. 3l), indicating its potential for use in robust and flexible energy storage devices. These findings confirm its promising application prospects.

The electrochemical measurements of the fabricated rCSCTN-1, -2, -3 and -4 electrodes were performed in a 6 M KOH alkaline electrolyte using a three-electrode configuration. Furthermore, the measurements were conducted within an optimized voltage range of 0 to 0.5 V. As seen from Fig. 4a, the CV curves of the fabricated rCSCTN-1, -2, -3 and -4 working electrodes at a scan rate of 100 mV s^{-1} all exhibited a pair of redox peaks. Additionally, rCSCTN-4 was found to have the largest circled area, which surpassed those of the other electrodes, indicating the highest redox activity among these samples. Fig. 4b depicts the corresponding GCD curves of all the working electrodes at a charge–discharge current density of 1 A g^{-1}, among which the discharge time of rCSCTN-4 was the longest. According to eqn (S1),† the specific capacitances of each electrode were calculated based on the GCD data, and the results were 655.6, 507.6, 353.2 and 1066 F g^{-1} (327.8, 253.8, 176.6 and 533 C g^{-1}), the specific capacitances of rCSCTN-1, -2 and -3 being evidently lower than that of rCSCTN-4. Moreover, the CV curves at different scan rates were obtained using scan rates ranging from 20 mV s^{-1} to 100 mV s^{-1} for the sake of further exploring the electrochemical properties of the rCSCTN-4 electrode.

As seen from Fig. 4c, the CV curves of rCSCTN-4 at various scan rates all exhibit similar curved shapes, indicating the remarkable reversibility and exceptional ion and electron transport capabilities.[54,55] Fig. 4d shows the GCD curves of the fabricated rCSCTN-4 electrode. As the current density increases from 1 to 5 A g^{-1}, the GCD curves exhibited an increasingly decreasing discharging time. Notably, the GCD curves of the fabricated electrode with symmetrical distribution at different current densities demonstrate its excellent reaction reversibility. Additionally, as depicted in Fig. S7a, b–S9a and b,† the trend and contour variation of CV and GCD curves of each comparison electrode are similar to those of the rCSCTN electrode. Fig. S7c–S10c† depict the capacitance retentions of rCSCTN-1, -2, -3 and -4 electrodes. Apparently, rCSCTN-4 has the best capacitance, retaining 90.96% of its initial capacity, which far exceeds the capacitance retention of the others. Furthermore, Fig. 4e exhibits specific capacitances of the rCSCTN-4 electrode at various current densities of 1, 2, 3, 4 and 5 A g^{-1}, which are 1066, 1028, 984, 976 and 960 F g^{-1} (533, 514, 492, 488 and 480C g^{-1}) as calculated from eqn (S1),† respectively. The specific capacitance of rCSCTN-4 was evidently greater than that of the other samples at the same current density. Fig. 4g depicts the specific capacitance of rCSCTN-4 electrode at a current density of 1 A g^{-1}, which is much larger than those recently reported for graphene-based electrode materials.[56–59]

Fig. 4f compares the Nyquist plots of EIS spectra of rCSCTN-1, -2, -3 and -4. The charge transfer resistance (R_{ct}) is related to the diameter of the semicircle. The internal resistance (R_s) is correlated with the intercept of the curve on the *x*-axis, and the internal resistance includes the prepared electrode material resistance and ion diffusion resistance between the prepared electrode material and the current collector. Thus, it can be noticed that rCSCTN-1, -2, -3 and -4 have R_s values of 0.60 Ω, 0.70 Ω, 0.86 Ω and 0.58 Ω. As a result, rCSCTN-4 has the lowest internal resistance, the highest conductivity and superior capacitive performance. The impedance curve of the rCSCTN-4 electrode exhibits a steep low-frequency slope, indicating that it has a low diffusion resistance during Faraday redox. The diffusion resistance (R_w) of rCSCTN-4 is lower than those of the

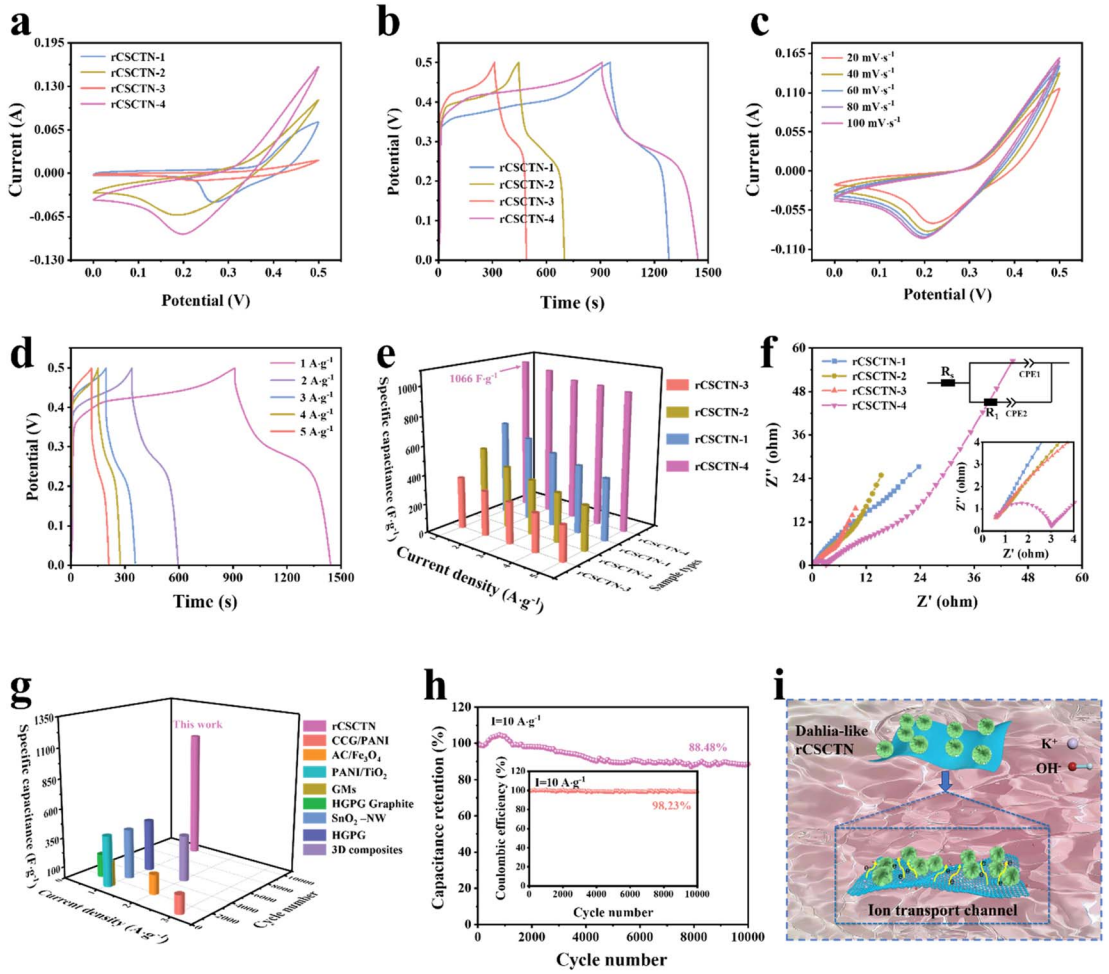

Fig. 4 (a) CV curves of rCSCTN-1, rCSCTN-2, rCSCTN-3 and rCSCTN-4 electrodes. (b) GCD curves of rCSCTN-1, -2, -3 and -4 electrodes. (c) CV and (d) GCD curves of rCSCTN-4 electrode measured at numerous scan rates and current densities, respectively. (e) The capacitive performance of all the manufactured electrodes. (f) Nyquist plots of rCSCTN-1, -2, -3 and -4 electrodes. (g) Comparison of the specific capacitances of rCSCTN-4 electrode with those of newly reported materials that are similar. (h) Coulombic efficiency and cyclic stability of the rCSCTN electrode at 10 A g^{-1}. (i) Diagrammatic representation explaining the mechanisms underlying the rCSCTN-4 electrode's improved electrochemical performance.

other electrodes. Thus, rCSCTN-4 has better capacitive performance compared with rCSCTN-1, -2 and -3. Furthermore, Fig. 4h illustrates the capacitance retention of the rCSCTN-4 electrode. Apparently, the rCSCTN-4 electrode demonstrates superior capacitance, retaining 88.48% of its initial capacity. In addition, the coulombic efficiency of the rCSCTN-4 electrode is up to 98.23%.

In addition, Fig. 4i shows a schematic diagram explaining why the rCSCTN-4 electrode exhibits excellent supercapacitor performance and cycling stability. By constructing complex nanostructures, the actual specific capacitance of traditional two-dimensional (2D) materials such as graphene has been improved, and the synergistic effect of different components has been enhanced. The multiple components of the core–shell structure make its electrochemical performance far superior to that of a single material. Firstly, rGO as a substrate has excellent conductivity, and the constructed core–shell structured nanomaterials have a large specific surface area, significantly improving the electrochemical performance of electrode materials. Secondly, the CSCTN dahlia-like structure forms a large accessible transportation network, promoting the diffusion of electrolytes. The rich open space formed between the core–shell nanosheets can serve as an "ion buffer memory", fully utilizing the electrode active material, reducing the diffusion resistance of electrolyte ions, and enabling the electrolyte to rapidly diffuse into the internal area of the electrode through the inverse Faraday reaction. Therefore, the rCSCTN-4 electrode material can achieve greater specific capacitance, better rate capability, and longer lifespan, thanks to the unique structure and synergistic effect generated by its multi-component composition.[60]

For the purpose of further elucidating the electrochemical properties and energy storage theory of the rCSCTN electrodes, CV curves at multiple scanning rates of 1, 3, 5, 7 and 9 mV s^{-1} were measured as depicted in Fig. S12a–S15a.† We used the following calculations and electrochemical tests to investigate these samples' charge storage process.

$$i = av^b \quad (1)$$

$$i = k_1 v + k_2 v^{1/2} \quad (2)$$

where v stands for sweep speed, i for current, a and b are fitting constants from Fig. 5a–c and S11;† k_1 and k_2 computed from the aforementioned equations are unchangeable. When the value of b is 0.5, the prepared electrode material conforms to the principle of diffusion control behaving as a complete battery. Meanwhile, the produced electrode material exhibits complete capacitive behavior conforming to the principle of capacitive control when the constant b is 1. In addition to this, when the value of b is between 0.5 and 1, the electrode at this point has both capacitive and battery behavior. On the whole, the magnitude of b plays a decisive role in the electrochemical behavior of the electrode. As is illustrated in Fig. 5a–c and S11,† the values of b of the anode peaks of prepared rCSCTN-1, rCSCTN-2, rCSCTN-3 and rCSCTN-4 electrodes are as follows: 0.58, 0.60, 0.65 and 0.72. Additionally, the cathode peaks' numerical results for b are, in that order, 0.57, 0.66, 0.62, and 0.62. This result reveals that the electrodes exhibit both diffusion and capacitive control principles. Furthermore, the contributions of diffusion or capacitive control behavior of the prepared electrodes are calculated through eqn (1) and (2) as depicted in Fig. 5d–f and S12d–S15d† at 5 mV s^{-1} sweep speed. Fig. S12–S15b–f† show the capacitance contribution rates of the rCSCTN electrodes when the sweep speeds are 1, 3, 5, 7 and 9 mV s^{-1}, respectively. As shown in Fig. 5g–i and S16,† the contribution of the capacitive-controlled principle is greater as the sweep rate increases. This phenomenon is attributed to the fast sweep speed, high current density and limitation of ion diffusion inside the electrode.

In order to meet the high-capacity requirements of flexible energy storage devices in daily life, we have constructed ASC series and parallel devices separately to test the integration performance of the devices. By connecting two identical ASC devices in series and parallel, it can be seen that the charging/discharging time as well as the working voltage are doubled respectively (Fig. S17†). This proves the excellent integration performance of the prepared ASC devices. Moreover, an ASC device was assembled with AC-coated nickel foam as the negative

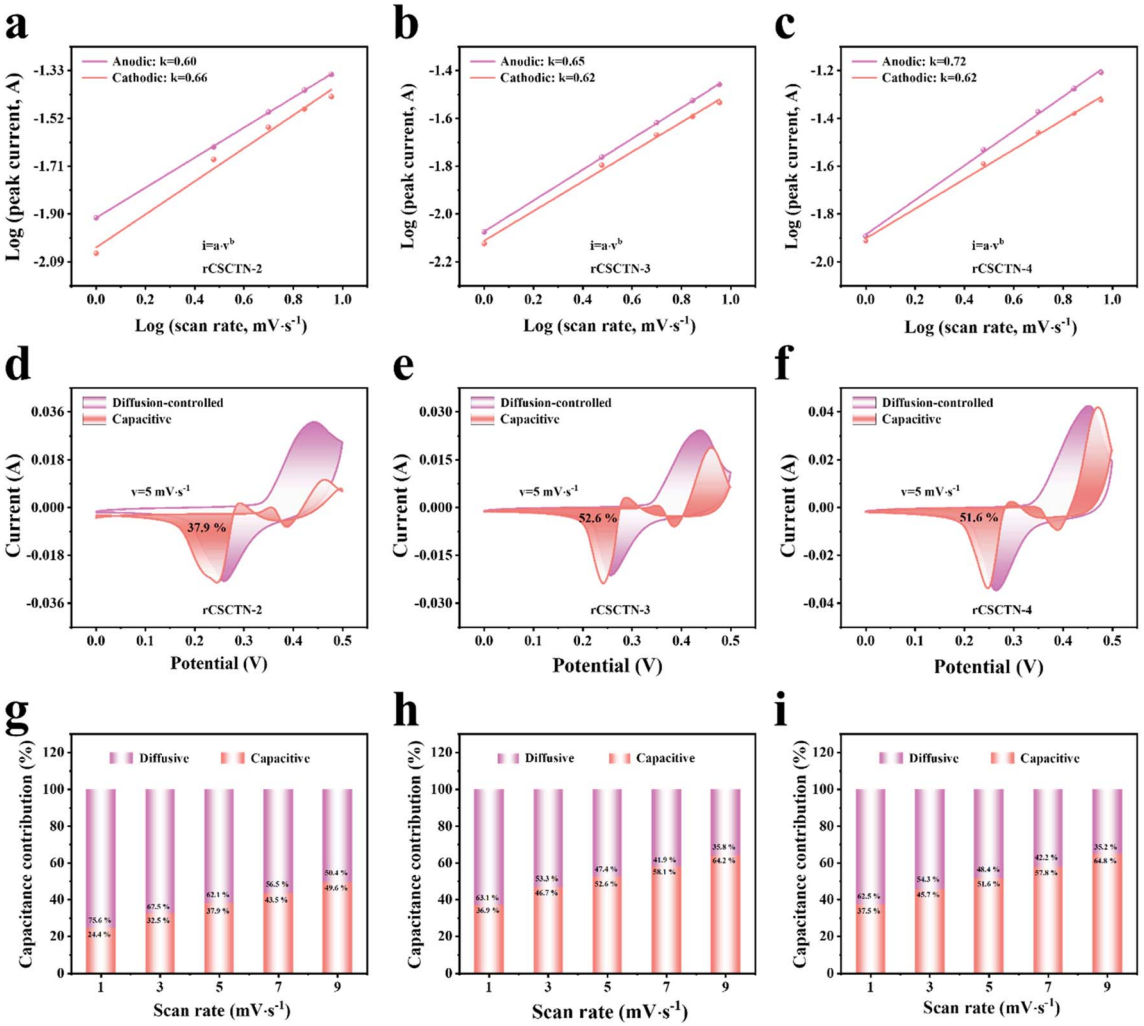

Fig. 5 Electrochemical behavior studies of the rCSCTN electrodes. Plots of logv and log$i$ of the (a) rCSCTN-2, (b) rCSCTN-3 and (c) rCSCTN-4 electrodes. Contributions from diffusion and capacitance to the charge storage of the electrodes at 5 mV s^{-1} for (d) rCSCTN-2, (e) rCSCTN-3 and (f) rCSCTN-4 electrodes. Capacitance contribution rates of (g) rCSCTN-2, (h) rCSCTN-3 and (i) rCSCTN-4 electrodes at multiple scan rates.

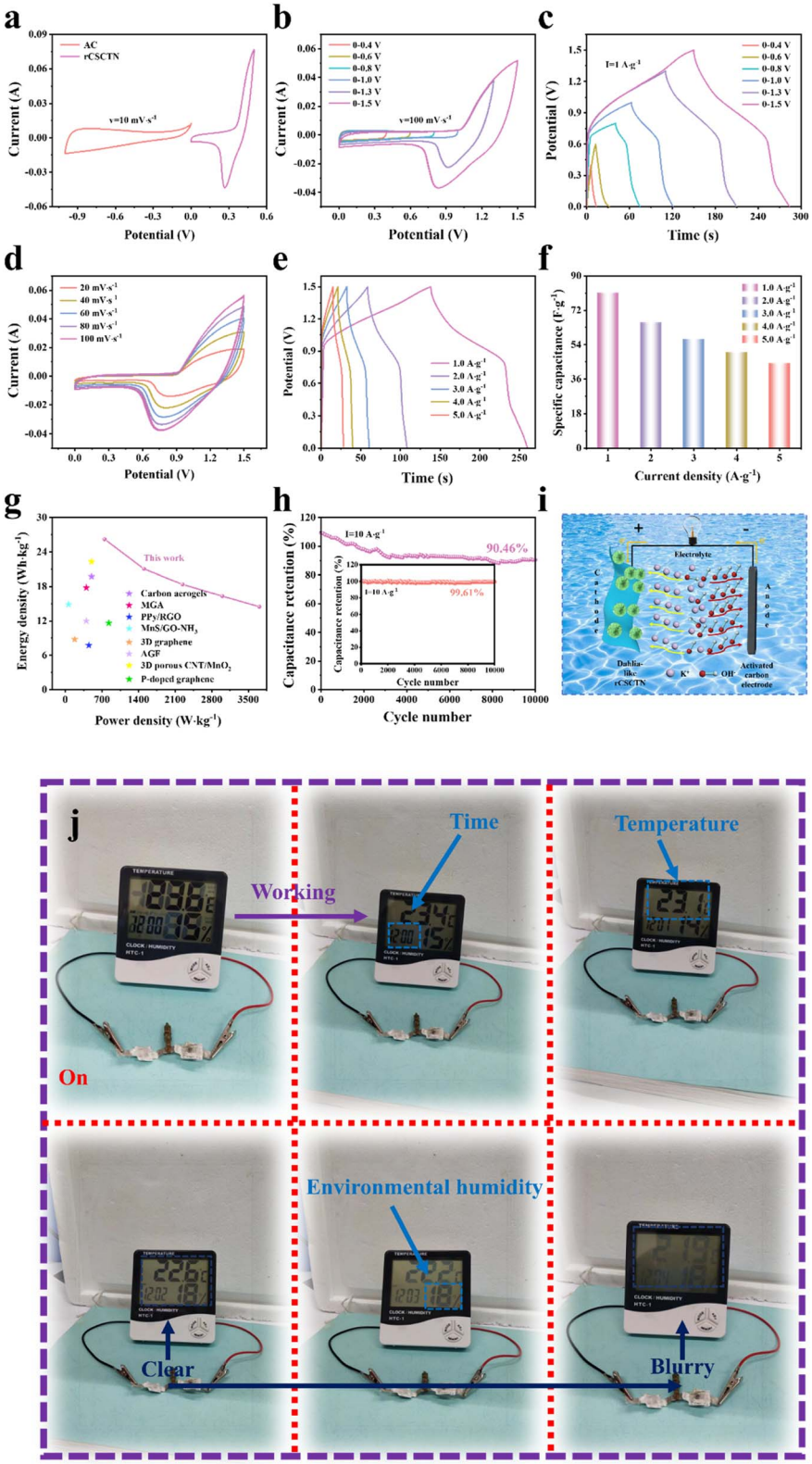

Fig. 6 (a) CV curves of AC and rCSCTN-4 electrode. (b) CV curves in various potential windows at 100 mVs^{-1} sweep speed. (c) GCD curves of rCSCTN-4 in various voltage windows at a current density of 1 Ag^{-1}. (d) ASC's CV curves at various scan speeds. (e) ASC's GCD curves for multiple current densities. (f) The capacitance property of ASC at multiple current densities. (g) A comparison of the rCSCTN-4//AC asymmetric supercapacitor device's Ragone plot with those already published in the literature. (h) Stability of cycling of the rCSCTN-4 electrode at 10 A g^{-1} current density (coulombic efficiency is displayed in the inset). (i) Illustration of the ASC device's operation theory. (j) Two solid-state ASCs connected in series powered a domestic temperature and humidity meter's LED screen for a duration of 12 minutes.

electrode and rCSCTN-4 as the positive electrode to further investigate the practical performance.[61–63] The three-electrode system's rCSCTN-4 electrode and AC electrode CV curves are depicted in Fig. 6a. The GCD and CV curves of the rCSCTN//AC ASC device, obtained in different voltage windows, are displayed in Fig. 6b and c. The CV and GCD curves essentially have the same forms when the potential window is between 0 and 1.5 V. Additionally, the curves' enclosed area progressively grows, indicating that the constructed equipment has a rather steady capacitance. Fig. 6d and e displays the CV and GCD curves of rCSCTN//AC devices at diverse scanning rates and various current densities. As can be seen from Fig. 6f, the rCSCTN//AC device displays excellent specific capacitances of 81.07, 65.73, 56.8, 50.13 and 44.33 F g^{-1} (40.54, 32.87, 28.4, 25.07 and 22.17 C g^{-1}) at 1, 2, 3, 4 and 5 A g^{-1}, correspondingly. Additionally, using eqn (S3) and (S4),† the energy density of rCSCTN-4 was determined to be 26.21 W h kg^{-1} at a power density of 748.86 W kg^{-1}.

Fig. 6g displays Ragone plots of rGO-based electrode materials reported before. This work clearly demonstrates higher power and energy densities. Hence, rCSCTN-4 exhibits excellent electrochemical performance compared with other materials.[64–68] From Fig. 6h we can see that the rCSCTN//AC ASC device displays excellent stability (90.46%) after 10 000 cycles. At 10 A g^{-1} current density, the produced electrode's coulombic efficiency can maintain up to 99.61%. SEM and XRD results of rCSCTN after cycling are shown in Fig. S19.† Additionally, a schematic representation of the assembled ASC apparatus is shown in Fig. 6i, where the electrode serves as the cathode and the AC electrode as the anode. The integrated device has a quick discharge–charge velocity due to the quick movement of OH^- and K^+ between the anode and cathode. In addition, from the point of view of practical application, the assembled ASC device, as can be seen from Fig. 6j, could power a LED screen for 12 min, further manifesting the promising practical application. To sum up, in practical applications, the synthesized rCSCTN is anticipated to be a viable option for electrodes with exceptional capacitive performance in energy storage devices.

3. Conclusions

In conclusion, rCSCTN, a dahlia-like core–shell structured composite, was successfully synthesized utilizing rGO as the template precursor in a simple two-step hydrothermal process for a supercapacitor electrode. With a specific capacitance of 1066 F g^{-1} (533 C g^{-1}) at a current density of 1 A g^{-1}, the rCSCTN electrode performs very well and shows remarkable rate capabilities and cycling stability, attributed to quantities of nanosheets arranged on rCTC with significantly expanded specific surface area. The capacitance retention rate reaches up to 90.46% after 10 000 cycles at a current density of 10 A g^{-1}. Furthermore, in 6.0 KOH aqueous electrolyte at an operating voltage of 1.5 V, the built supercapacitor device displays a power density of 748.86 W kg^{-1} at an energy density of 26.21 W h kg^{-1}. The assembled ASCs (rCSCTN//AC) can supply electricity to a domestic LED screen for 12 minutes, demonstrating the application potential of the rCSCTN composite in its current state. Furthermore, a PVA/KOH gel-electrolyte was used to produce a flexible and highly tensile rCSCTN/PVA/KOH film electrode that can be twisted into a variety of shapes and bent at different angles. The rCSCTN/PVA/KOH film is clearly able to lift a 500 mL (500 g) plastic jar filled with water, showcasing its excellent application potential for durable and wearable electronic equipment. In order to produce graphene- and tin-based chalcogenide core–shell electrode composites that resemble dahlias for use in supercapacitors and flexible devices for storing energy, this ground-breaking discovery provides fresh ideas. Overall, the produced material has outstanding electrochemical performance, and this work will provide insight into the development of electrodes with exceptional capacitance properties for storage of energy in real-world usage.

4. Experimental

4.1 Reagents

There was no need for additional purification because the reagents utilized were analytically pure. A Boko SCSJ-II-40L ultrapure water machine provided ultrapure water. The supplier of nickel foam (NF) was Shenzhen Zhida Environmental Technology Co. Ltd Qingdao Jinhui Graphite Co. Ltd supplied the expanded graphite. Sinopharm Chemical Reagent Co. Ltd supplied the following: sulfuric acid (H_2SO_4, AR), hydrochloric acid (HCl, AR), potassium permanganate ($KMnO_4$, AR), hydrogen peroxide (H_2O_2, AR), tin(II) chloride dihydrate ($SnCl_2 \cdot 2H_2O$, AR), nickel(II) chloride hexahydrate ($NiCl_2 \cdot 6H_2O$, AR), cobalt chloride hexahydrate ($CoCl_2 \cdot 6H_2O$, AR), urea (CH_4N_2O, AR), thioacetamide (TAA, AR), absolute ethanol (CH_3CH_2OH, AR), potassium hydroxide (KOH, AR), acetylene black (ACET, AR), polyvinyl alcohol 1750 ± 50 (PVA, AR), activated carbon (AC, AR) and polyvinylidene fluoride (PVDF, AR).

4.2 Synthesis of dispersions of graphene oxide (GO)

With certain adjustments, the Hummers approach was used to prepare GO dispersions.[69,70] Typically, 400 mL of concentrated H_2SO_4 was added to 5 g of expanded graphite while it was being stirred. Following a 24 hours period of stirring, $KMnO_4$ (25 g) was gradually added while stirring and the mixture was cooled to maintain a temperature below 20 °C. The mixture was then stirred for 24 h, and 300–400 mL of DI water was gradually added to the mixture. The liquid turned a brilliant yellow once the reaction ceased by adding an excess quantity of 30% H_2O_2 solution after stirring for 24 hours. To get rid of the metal ions, the mixture was passed through filters and cleaned with DI water and 10% HCl solution after standing for 24 hours. The GO product was suspended in DI water to create a thick brown dispersion. The metal ions and acids were then totally removed from the dispersion using dialysis. In order to facilitate further tests, GO dispersions' concentration was finally prepared at 10 mg mL^{-1}.

4.3 Synthesis of cobalt/tin-based chalcogenide grown on reduced graphene oxide (rCTC)

Firstly, 10.4 mL previously prepared GO dispersion was diluted to 80 mL, then sonicated for 40 min to disperse the GO evenly.

The obtained GO dispersion was then poured evenly into four beakers. Moreover, 1.06 g, 0.25 g, 0.18 g and 1.06 g $SnCl_2 \cdot 2H_2O$ were added to the four beakers that had equal amounts of $CoCl_2 \cdot 6H_2O$ (0.014 g) and TAA (0.136 g), respectively. The contents of the four bakers were then each dissolved in 15 mL of ultrapure water and then magnetically stirred for 20 min. After that, the previously dispersed GO dispersions were mixed with the above four solutions in the beakers, and then heated for 6 hours at 160 °C. After the hydrothermal treatment, Co-doped SnS nanoparticles were formed on the surface of rGO to afford rCTC-1, rCTC-2, rCTC-3 and rCTC-4, respectively.

4.4 Synthesis of rCSCTN composites

0.2 g, 0.3 g, 0.3 g and 0.1 g of $NiCl_2 \cdot 6H_2O$ were added into the rCTC-1, rCTC-2, rCTC-3 and rCTC-4 solutions obtained by the first hydrothermal reaction, respectively. Additionally, each resulting solution was supplemented with an equivalent quantity of urea (0.15 g) and kept at 100 °C for two hours, and then rCSCTN-1, rCSCTN-2, rCSCTN-3 and rCSCTN-4 were obtained by vacuum filtration and freeze-drying.

Data availability

The data supporting this article have been included as part of the ESI.†

Author contributions

Huiru Sun: conceptualization, visualization, formal analysis, writing – original draft. Hanwen Zong: methodology, validation, writing – review & editing. Wenjun Huang: supervision, writing – review & editing. Lejiao Duan: visualization, software. Jingjing Dong: data curation. Yuesheng Sun: investigation. Zhongqi Lu: visualization. Zhihan Yang: investigation. Yawen Liu: software. Jingquan Liu: resources, project administration, funding acquisition, writing – review & editing.

Conflicts of interest

There are no conflicts to declare.

Acknowledgements

This work was supported by Double-Hundred Foreign Experts Program of Shandong Province and National Natural Science Foundation of China (21805124). The authors would like to thank Xiaoli Fan from Shiyanjia Lab (**www.shiyanjia.com**) for the TEM analysis.

References

1 Z. B. Zhai, W. Yan, L. Dong, J. Y. Wang, C. H. Chen, J. Lian, X. M. Wang, D. G. Xia and J. J. Zhang, *Nano Energy*, 2020, **78**, 105193.
2 I. Oh, M. Kim and J. Kim, *Energy*, 2015, **86**, 292–299.
3 A. T. Zhang, N. Mao, Y. X. Zhong, W. Zheng, L. Cui, C. Barrow, J. Razal, W. R. Yang and J. Q. Liu, *Composites, Part B*, 2021, **215**, 108756.
4 H. C. Fu, A. T. Zhang, F. H. Jin, H. W. Guo and J. Q. Liu, *ACS Appl. Mater. Interfaces*, 2022, **14**, 16165–16177.
5 J. Dong, H. Peng, J. Wang, C. Wang, D. Wang, N. Wang, W. Fan, X. Jiang, J. Yang and Y. Qian, *Energy Stor. Mater.*, 2023, **54**, 875–884.
6 H. Zong, A. Zhang, J. Dong, Y. He, H. Fu, H. Guo, F. Liu, J. Xu and J. Liu, *Chem. Eng. J.*, 2023, **475**, 146088.
7 C. Z. Wei, Q. Y. Chen, C. Cheng, R. Liu, Q. Zhang and L. P. Zhang, *Inorg. Chem. Front.*, 2019, **6**, 1851–1860.
8 C. Z. Wei, R. Zhang, X. Zheng, Q. L. Ru, Q. Y. Chen, C. Cui, G. Li and D. J. Zhang, *Inorg. Chem. Front.*, 2018, **5**, 3126–3134.
9 Z. X. Shi, Y. Liu, Y. C. Zhang, J. Sun, J. X. Zheng, C. Z. Wei, W. M. Du, L. Liu and C. Cheng, *Appl. Surf. Sci.*, 2023, **611**, 155758.
10 Y. Hu, H. H. Cheng, F. Zhao, N. Chen, L. Jiang, Z. H. Feng and L. T. Qu, *Nanoscale*, 2014, **6**, 6448.
11 C. Ogata, R. Kurogi, K. Hatakeyama, T. Taniguchi, M. Koinuma and Y. Matsumoto, *Chem. Commun.*, 2016, **52**, 3919.
12 C. X. Shao, T. Xu, J. Gao, Y. Liang, Y. Zhao and L. T. Qu, *Nanoscale*, 2017, **9**, 12324.
13 M. B. Tayel, M. M. Soliman, S. Ebrahim and M. E. Harb, *Synth. Met.*, 2016, **217**, 237–243.
14 Y. L. Shao, J. M. Li, Y. G. Li, H. Z. Wang, Q. H. Zhang and R. B. Kaner, *Mater. Horiz.*, 2017, **4**, 1145–1150.
15 P. Y. Tang, L. J. Han and L. Zhang, *ACS Appl. Mater. Interfaces*, 2014, **6**, 10506–10515.
16 V. J. Mane, S. B. Kale, S. B. Ubale, V. C. Lokhande and C. D. Lokhande, *Mater. Today Chem.*, 2021, **20**, 100473.
17 M. P. Down, S. J. Rowley-Neale, G. C. Smith and C. E. Banks, *ACS Appl. Energy Mater.*, 2018, **1**, 707–714.
18 P. Ahuja, S. K. Ujjain and R. Kanojia, *Appl. Surf. Sci.*, 2018, **427**, 102–111.
19 Z. Q. Lu, K. Zhao, H. W. Guo, L. J. Duan, H. R. Sun, K. Y. Chen and J. Q. Liu, *Small*, 2023, **20**, 2309814.
20 C. Li, D. Jiang, H. Liang, B. Huo, C. Liu, W. Yang and J. Liu, *Adv. Funct. Mater.*, 2018, **28**, 1704674.
21 X. Y. Cao, X. X. Wang, L. Cui, D. G. Jiang, Y. W. Zheng and J. Q. Liu, *Chem. Eng. J.*, 2017, **327**, 1085–1092.
22 N. N. Chen, L. Ni, J. H. Zhou, G. Y. Zhu, Q. Kang, Y. Zhang, S. Y. Chen, W. X. Zhou, C. L. Lu, J. Chen, X. M. Feng, X. Z. Wang, X. F. Guo, L. M. Peng, W. P. Ding and W. H. Hou, *ACS Appl. Energy Mater.*, 2018, **1**, 5189–5197.
23 Z. S. Wu, W. C. Ren, D. W. Wang, F. Li, B. L. Liu and H. M. Cheng, *ACS Nano*, 2010, **4**, 5835–5842.
24 H. W. Guo, A. T. Zhang, H. C. Fu, H. W. Zong, F. H. Jin, K. Zhao and J. Q. Liu, *Chem. Eng. J.*, 2023, **453**, 139633.
25 P. C. Du, X. W. Hu, C. Yi, H. C. Liu, P. Liu, H. L. Zhang and X. Gong, *Adv. Funct. Mater.*, 2015, **25**, 2420–2427.
26 Y. G. Wang and Y. Y. Xia, *Adv. Mater.*, 2013, **25**, 5336–5342.
27 Y. Yoon, K. Lee, C. Baik, H. Yoo, M. Min, Y. Park, S. M. Lee and H. Lee, *Adv. Mater.*, 2013, **25**, 4437–4444.
28 L. L. Liu, Z. Q. Niu and J. Chen, *Chem. Soc. Rev.*, 2016, **45**, 4340–4363.

29 J. R. Tian, Z. F. Yang, Z. F. Yin, Z. Z. Ye, J. Wang, C. J. Cui and W. Z. Qian, *Chem. Rec.*, 2019, **19**, 1256–1262.
30 J. T. Zhang, J. W. Jiang, H. L. Li and X. S. Zhao, *Energy Environ. Sci.*, 2011, **4**, 4009–4015.
31 M. J. Allen, V. C. Tung and R. B. Kaner, *Chem. Rev.*, 2010, **110**, 132–145.
32 H. F. Su, T. Wang, S. Y. Zhang, J. M. Song, C. J. Mao, H. L. Niu, B. K. Jin, J. Y. Wu and Y. P. Tian, *Solid State Sci.*, 2012, **14**, 677–681.
33 R. Lakra, R. Kumar, P. K. Sahoo, D. Thatoi and A. Soam, *Inorg. Chem. Commun.*, 2021, **133**, 108929.
34 G. B. Pour, L. F. Aval and M. Mirzaee, *J. Mater. Sci.: Mater. Electron.*, 2018, **29**, 17432–17437.
35 Q. Cheng, J. Tang, N. Shinya and L. C. Qin, *Sci. Technol. Adv. Mater.*, 2014, **15**, 014206.
36 S. P. Lim, N. M. Huang and H. N. Lim, *Ceram. Int.*, 2013, **39**, 6647–6655.
37 J. Zou, S. Zhang, Y. Huang, J. Wang, X. Liu, S. Zhang, Y. Gao, C. Chen and M. Yu, *J. Alloys Compd.*, 2023, **965**, 171400.
38 P. I. John, G. Vaitheeswaran, R. Venkatesan, R. Nagalingam, M. Jeyanthinath and N. Perumal, *J. Energy Storage*, 2023, **70**, 107952.
39 W. J. Huang, A. T. Zhang, H. C. Fu, M. Z. Zhang, W. T. Cheng, C. J. Barrow, W. R. Yang and J. Q. Liu, *Chem.–Eur. J.*, 2021, **27**, 17402–17411.
40 X. Bai, Q. Liu, J. Y. Liu, H. S. Zhang, Z. S. Li, X. Y. Jing, P. L. Liu, J. Wang and R. M. Li, *Chem. Eng. J.*, 2017, **315**, 35–45.
41 Z. Y. Zhan, S. J. Chen, J. L. Xie, Y. F. Yang and J. Xiong, *J. Alloys Compd.*, 2017, **722**, 928–937.
42 Y. W. Liu, C. X. Wang, Y. Liu, Z. H. Yang, Z. X. Wang and J. Q. Liu, *Electrochim. Acta*, 2024, **488**, 144151.
43 C. Z. Wei, J. Sun, Y. C. Zhang, Y. Liu, Z. C. Guo, W. M. Du, L. Liu and Y. M. Zhang, *Inorg. Chem. Front.*, 2022, **9**, 3542–3551.
44 F. F. Cao, M. Y. Gan, L. Ma, X. R. Li, F. B. Yan, M. H. Ye, Y. F. Zhai and Y. Zhou, *Synth. Met.*, 2017, **234**, 154–160.
45 D. L. Li, Y. N. Gong, M. S. Wang and C. X. Pan, *Micro Nano Lett.*, 2017, **9**, 16.
46 Y. C. Pang, S. Y. Zhang, S. Chen, J. Liang, M. Y. Li, D. W. Ding and S. J. Ding, *Chem.–Eur. J.*, 2018, **24**, 16104–16112.
47 Y. F. Zhao, Y. F. Zhang, Y. Cheng, W. S. Zhao, W. J. Chen, C. G. Meng and C. Huang, *Mater. Lett.*, 2021, **282**, 128774.
48 S. R. Ede and S. Kundu, *ACS Sustainable Chem. Eng.*, 2015, **3**, 2321–2336.
49 M. Zhang, D. Lei, Z. F. Du, X. M. Yin, L. B. Chen, Q. H. Li, Y. G. Wang and T. H. Wang, *J. Mater. Chem.*, 2011, **21**, 1673–1676.
50 O. Akhavan, *ACS Nano*, 2010, **4**, 4174–4180.
51 H. L. Wang, J. T. Robinson, X. L. Li and H. J. Dai, *J. Am. Chem. Soc.*, 2009, **131**, 9910.
52 W. Lu, B. B. Xie, C. Yang, C. Tian, L. Yan, J. Q. Ning, S. Li, Y. J. Zhong and Y. Hu, *Small*, 2023, **19**, 2302629.
53 X. H. Chen, P. C. Ye, H. Y. Wang, H. Huang, Y. J. Zhong and Y. Hu, *Adv. Funct. Mater.*, 2023, **33**, 2212915.
54 B. Liu, H. J. Sun, T. J. Peng and X. Zhi, *Diamond Relat. Mater.*, 2021, **118**, 108498.
55 Y. T. Ma, Y. Y. Bai, B. P. Liang, R. F. Yang, X. Y. Jiang, S. Z. Zheng, C. Q. Zhang and C. Y. Hu, *Appl. Surf. Sci.*, 2022, **579**, 152156.
56 Q. Wu, Y. X. Xu, Z. Y. Yao, A. R. Liu and G. Q. Shi, *ACS Nano*, 2010, **4**, 1963–1970.
57 T. Van Ngo, M. Moussa, T. T. Tung, C. Coghlan and D. Losic, *Electrochim. Acta*, 2020, **329**, 135104.
58 Y. Chen, N. Wang, S. Han, M. Jensen, X. F. Li and X. X. Zhang, *Electrochim. Acta*, 2021, **383**, 138240.
59 Y. Wang, Z. Q. Shi, Y. Huang, Y. F. Ma, C. Y. Wang, M. M. Chen and Y. S. Chen, *J. Phys. Chem. C*, 2009, **113**, 13103–13107.
60 C. X. Wang, Y. W. Liu, Y. S. Sun, J. T. Xu and J. Q. Liu, *Appl. Surf. Sci.*, 2024, **653**, 159407.
61 M. K. Singh and S. A. Hashmi, *Ionics*, 2017, **23**, 2931–2942.
62 A. Bahaa, M. A. Abdelkareem, H. Al Naqbi, A. Y. Mohamed, P. A. Shinde, B. A. A. Yousef, E. T. Sayed, H. Alawadhi, K. J. Chae, S. Al-Asheh and A. G. Olabi, *J. Colloid Interface Sci.*, 2022, **608**, 711–719.
63 Z. Q. Li, X. X. Wang, M. D. Xu, Z. K. Yin and J. L. Zhao, *J. Alloys Compd.*, 2022, **894**, 162492.
64 P. Hao, Z. H. Zhao, J. Tian, H. D. Li, Y. H. Sang, G. W. Yu, H. Q. Cai, H. Liu, C. P. Wong and A. Umar, *Nanoscale*, 2014, **6**, 12120–12129.
65 J. B. Zhu, Y. L. Xu, J. Wang, J. Lin, X. F. Sun and S. C. Mao, *Phys. Chem. Chem. Phys.*, 2015, **17**, 28666–28673.
66 Y. F. Tang, T. Chen, S. X. Yu, Y. Q. Qiao, S. C. Mu, J. Hu and F. M. Gao, *J. Mater. Chem. A*, 2015, **3**, 12913–12919.
67 A. Ramadoss, K. Y. Yoon, M. J. Kwak, S. I. Kim, S. T. Ryu and J. H. Jang, *J. Power Sources*, 2017, **337**, 159–165.
68 A. Bello, F. Barzegar, D. Momodu, J. Dangbegnon, F. Taghizadeh and N. Manyala, *Electrochim. Acta*, 2015, **151**, 386–392.
69 K. Gopalakrishnan, A. Govindaraj and C. N. R. Rao, *J. Mater. Chem. A*, 2013, **1**, 7563–7565.
70 S. H. Hsieh, W. J. Chen and T. H. Yeh, *Ceram. Int.*, 2015, **41**, 13759–13766.

